ORIGINAL ARTICLE

Study on laser-MIG hybrid welding characteristics of A7N01-T6 aluminum alloy

Sang Liu[1] · Jianmin Li[1] · Gaoyang Mi[1] · Chunming Wang[1] · Xiyuan Hu[1]

Abstract In this paper, an experimental study of laser-metal inert gas (MIG) hybrid welding of A7N01-T6 aluminum alloy in butt joint configuration was carried out. Visual examination and optical microscope were utilized to study the macro profile and microstructure, while mechanical properties of the welds were evaluated with the help of a tensile test and microhardness measurement. The joints were evaluated by the scanning electron microscope (SEM) and energy dispersive X-ray spectroscopy (EDS). Besides, X-ray microtomography was employed to characterize the morphology, quantity, and distribution of porosities in the weld seam. The results revealed that 4-mm thickness high-quality laser-arc hybrid welding butt joints were obtained with parameters of laser power 3.5 kW, welding speed 4 m/min, and welding current 140 A. The average tensile strength of welded joints reached 268 MPa, 76.6 % of that of the base metal. The loss was likely to be related to the presence of micropores, and further three-dimensional characterization indicated that there were altogether 4326 pores with diameters ranging from 0.1 to 79 μm in the tested sample, accounting for 0.57 % of the volume fraction and 4.56 % of the cross-sectional area fraction at the most. The existence of porosities, the dissolution, and coarsening of strengthening precipitates together promoted the joint softening in A7N01-T6 hybrid welding process.

1 Introduction

Aluminum alloys are widely used as structural materials in different industries, such as transportable bridge girders, military vehicles, road tankers, and railway transport systems, due to their high strength-to-weight ratio characteristics, high resistance to corrosion, and good ductility even at subzero temperatures [1]. Introduction of such light material as bodies of cars and high-speed trains has become an important technology with the aim for higher efficiency. Presently, joints of aluminum alloys are preferred to be welded via the main methods of gas metal arc welding (GMAW), friction stir welding (FSW), electron beam welding (EBW), and hybrid laser-arc welding. GMAW is widely used to weld aluminum, but it may cause severe grain coursing and large deformation for excessive heat input [2]. FSW is one of the most important solid-state joining techniques and does not result in significant distortion or solute loss. Moreover, porosity in the cast condition can be healed by FSW. However, unreliable stirring tool wear and undefined mechanisms of microstructure evolution under complex processes and interactions still limit the development in industrial applications [3]. EBW could produce deep and narrow welds together with high efficiency and finer joint strength than traditional arc welding, but the vacuum atmosphere always imposes restrictions on workpiece shapes and dimensions [4]. As a relatively new fusion welding method, hybrid laser-arc welding has been considered to be a promising precision joining technique which absorbs the benefits afforded by the combination of a laser beam and an electric arc [5]. One of the heat sources can be gas metal arc welding

✉ Chunming Wang
   hustwangcm@sina.com; cmwang@mail.hust.edu.cn

1   School of Materials Science and Engineering, Huazhong University
    of Science and Technology, Wuhan 430074, People's Republic of
    China

Table 1 Chemical compositions of A7N01 and ER5356

Materials	Chemical composition (wt.%)								
	Si	Fe	Cu	Mn	Mg	Cr	Zn	Ti	Al
A7N01	0.08	0.19	0.16	0.41	1.26	0.17	4.35	0.031	Bal
ER5356	0.18	0.25	0.1	0.01	5.1	0.07	0.1	0.1	Bal

Table 2 The main process parameters in laser-MIG hybrid welding

Variable	Unit	Value
Laser power	kW	2.5, 3.0, 3.5, 4.0
Welding speed	m/min	3.0, 3.5, 4.0, 4.5, 5.0
MIG welding current	A	100, 120, 140, 160
Laser-arc distance	mm	2
Shielding gas flow (Ar)	m^3/h	1.5
Defocus amount	mm	−1

(GMAW) which can enhance the chemical composition stability of aluminum alloys and eliminate the metal oxide film with the effect of cathode cleaning mechanism. The other heat source is a laser beam which can yield enough penetration for thick workpieces and give higher efficiency and better surface quality after welding. When placed in a proper distance with each other, the two heat sources interact in such a way to generate a synergetic effect which has been showed to alleviate problems commonly encountered in a single process to some extent [6]. This method also gives more freedom for structural designers to use bigger gaps and has higher energy efficiency and process stability.

However, aluminum alloys behave rather poorly in terms of weldability. Problems like material loss by evaporation of low boiling point alloying elements magnesium and zinc, presence of hard aluminum oxide on the surface, distortion resulting from relatively high heat capacity, and hot cracks are standing in the way for good joint performance [7]. Especially, in age-hardened high-strength aluminum alloys, the thermal cycle during welding process would lead to hardness and strength undermatching in the weld for the annealing effect, even in the solid-state welding. The situation is even severe in fusion welding, for strengthening phases would be remelt and only cast materials with solute segregation and columnar grains remained [8]. What is worse, there are always lots of pores, including micropores and macropores, in the weld seam. First, the solubility of hydrogen in liquid metal is much higher than that in solid metal and hence dissolved gas are released during solidification, leading to the formation of pores. Pores resulting from solute gas are always

characterized by spherical shape and small size, often less than 1 μm and are called metallurgical porosities or micropores. The second kind of pores comes from that bubbles emerging at the bottom of the keyhole by intense evaporation and are easily trapped at the solidification front. This type of pores are characterized by relative huge size, often larger than 10 μm, and named process porosities or macropores, which can be restrained to a great extent via process parameter optimization [9–12]. A lot of research has been conducted on the formation of pores, but the relationships between pores and mechanical performances still remain a controversial issue. Shore and McCauley [13] conducted experiments on high-strength 7039 aluminum alloy, and results indicated that the loss in cross-sectional area due to porosity was proportional to the tensile strength while the effect was not so significant on yield strength. Rudy and Rupert [14] studied the effect of porosity on mechanical performance of aluminum welds and found that fine porosities, as well as large pores, would reduce strength when present in sufficient quantity. Gou et al. [15] studied the effect of humidity on porosity formation in A7N01S-T5 aluminum alloy weld and concluded that mean fatigue strength of welded joints reached the lowest level at the humidity of 70 %, under which condition the porosity had the maximum mean size, maximum diameter, maximum area, maximum total area, maximum sectional total area, and maximum possession rate.

In this work, the weldability of A7N01-T6 aluminum alloy with a hybrid laser-arc welding process was studied for the

Fig. 1 Experimental set-up for A7N01 hybrid welding. **a** Schematic diagram of welding configuration. **b** Clamping form of the welded plates
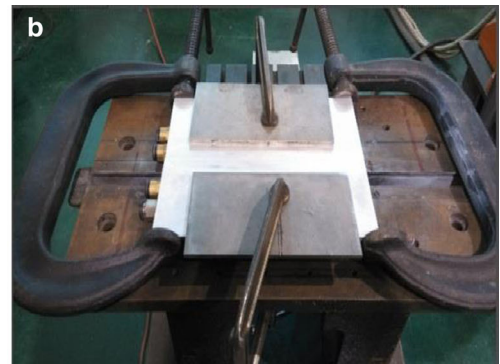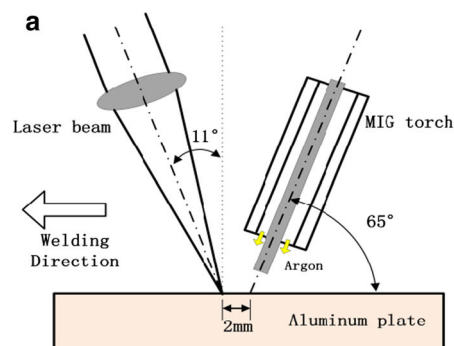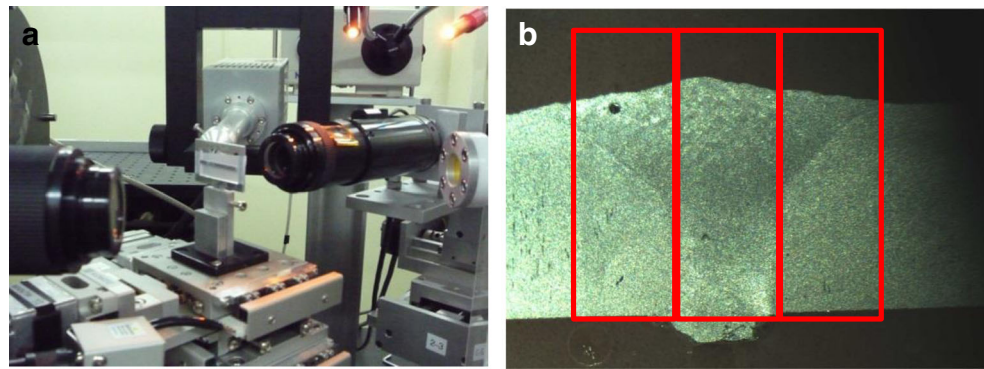
Fig. 2 Detection device **(a)** and testing sample **(b)** for three-dimensional porosity distribution

purpose of improving the microstructure and mechanical properties of the welds. Weld appearance was examined to evaluate weld quality using an optical microscope. Hardness and strength tests were carried out to identify mechanical properties of the laser-arc hybrid welded joint. Energy diffraction spectrum and synchrotron radiation X-ray microtomography were utilized to evaluate the element distribution and three-dimensional porosity distribution in the weld. Finally, fractography analyses with scanning electron microscopy were conducted with special attention on the porosities. Moreover, relevant mechanisms were also discussed.

2 Experimental procedures

The experimental materials were A7N01 alloy that had undergone T6 heat treatment (cooled from an elevated temperature during shaping process and then artificially aged) and ER5356 with a diameter of 1.2 mm as the filler metal considering the hot-crack tendency of high-strength A7N01 aluminum alloy. The chemical compositions are described in Table 1. Samples were all sheared into the same dimension of $100 \times 75 \times 4 \text{ mm}^3$. Before welding, the oxidation film and greasy dirt on the surface of substrates were eliminated by a series of mechanical and chemical cleaning methods.

The experiments were carried out with an IPG YLR-4000 fiber laser with a peak power of 4.0 kW, an ABB IRB4400 robot, and a Fronius TPS4000 arc welding machine. To avoid possible damages to the optical components, laser beam was inclined with an angle of 11° to the welding direction while the angle between welding torch and the specimen was set to 65°. The composite way of laser prior to arc was used in the welding process. The specific experimental set-up is presented in Fig. 1. The workpieces were pressed tightly together using jigs. Argon was used as the shielding gas for the top surface of the weld, and other welding process variables based on preliminary experience accumulation are showed in Table 2.

After welding, the samples were cut transversely from the welds by wire cutting, and then mechanically grinded and polished to obtain a mirror plane. The Keller's reagent (1 ml HF + 1.5 ml HCl + 2.5 ml HNO_3 + 95 ml H_2O) was used to etch the sample. Morphology observation was used to select the optimal combinations of welding parameters leading to good appearance without obvious defects. The element distributions within the joints were then analyzed via energy diffraction spectrum (EDS). Based on 13W1 beamline and station of the Shanghai Synchrotron Radiation Facility, three-dimensional (3D) porosity distributions of welded joints were reconstructed. The detection device and testing sample are presented in Fig. 2. Samples ($4 \times 4 \text{ mm}^2$) with weld cross section in the center were ground and polished to a 2-mm thickness, and a maximum energy of 20 KeV was adopted to ensure a 30 % transmission rate. Considering the mass data obtained and calculating efficiency, scanning area was divided into three parts firstly. Then, they were scanned step by step at 13W1 equipped with high-resolution X-ray CCD detector to obtain two-dimensional images through computed tomography (CT). After refactoring and gray level transformation, the images were recombined together via a 3D restructuring software named Amira to acquire the
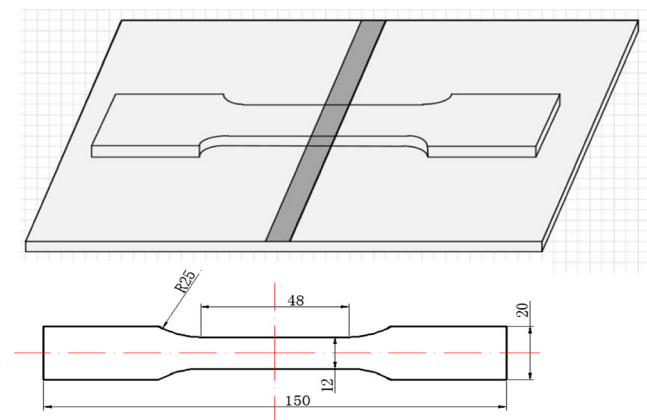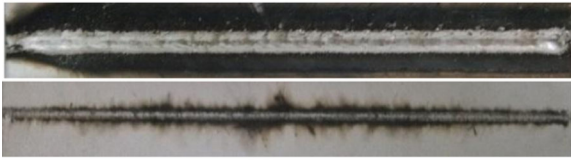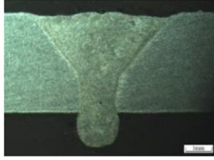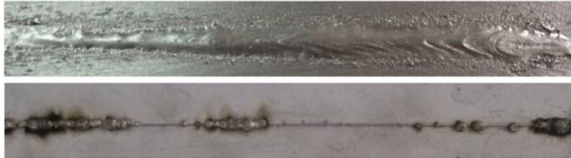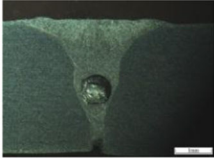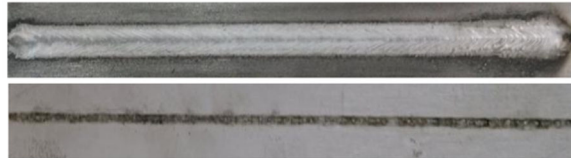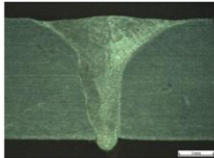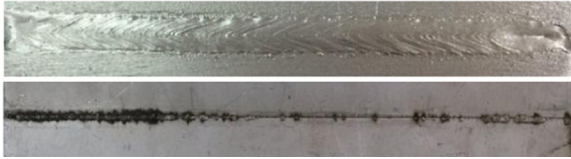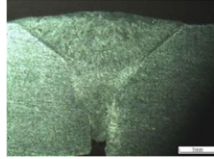

Fig. 3 Dimensions of the tensile-shear specimen

Table 3 Typical weld morphology

| Number	Process variables	Weld surface appearance	Cross section
1	P = 4 kW V = 4 m/min I = 140 A		
2	P = 3.8 kW V = 6 m/min I = 140 A		
3	P = 3.5 kW V = 4 m/min I = 140 A		
4	P = 3.5 kW V = 4 m/min I = 120 A		

porosity distribution of the joints intuitively and measurably. Vickers microhardness measurement was taken from the weld zone (WZ), passing through the heat-affected zone (HAZ), to the base metal (BM) with a spacing of 0.2 mm using a load of 0.98 N, and a dwell time of 10 s. Full-size transverse tensile specimens were machined from welded plates with the optimal processing parameters. The dimensions of the specimen are presented in Fig. 3.

3 Results and discussion

3.1 Morphology inspection

As shown in Table 3, a series of parameter combinations was examined for butt-welding of A7N01 workpieces and typical weld morphologies were obtained. Visual examinations of weld surface appearance were first performed, and results demonstrated that the welds produced by hybrid welding could have a

Fig. 4 Microstructure of A7N01 hybrid welding joint. **a** Fusion transition zone. **b** Weld center zone
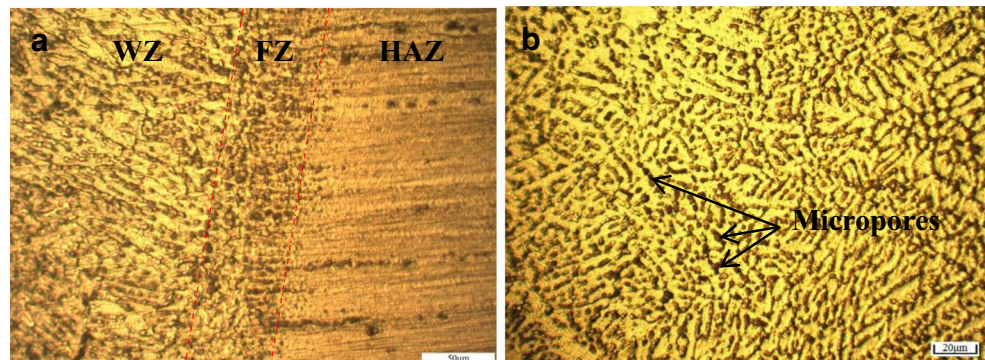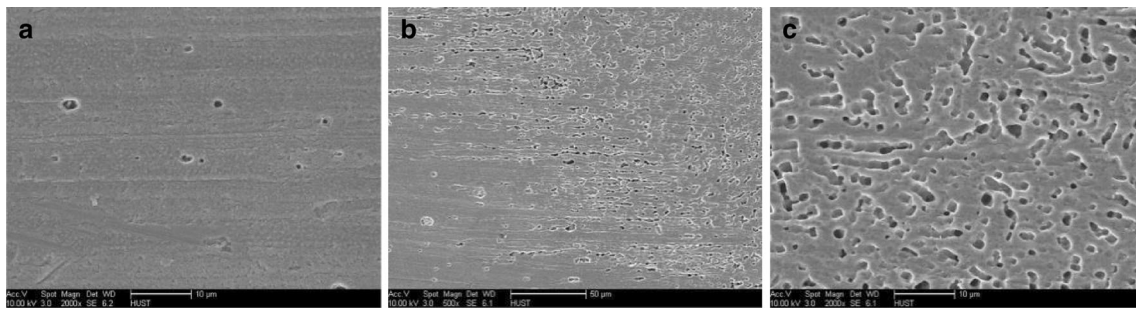
Fig. 5 SEM images of pore distribution in A7N01 hybrid welding joint. **a** BM. **b** Fusion transition zone. **c** Weld center zone

smooth top and regular root surface presented by sample no. 3. Characteristic wave lines on the surface, which are always considered to reflect a stable flow structure in the weld pool [16], could also be discovered. Observation of cross-sectional profiles indicated that funnel-shaped butt weld joints, which consisted of upper wide zones of laser-arc active region and lower narrow zones of nearly single-laser active region, were achieved with a small reinforcement on the top. Grains grew from both sides of the weld to the weld center, forming the so-called transgranular organization with a vague bonding line in the weld center. Columnar crystals should be found in the weld zone, and this will be discussed later. No obvious imperfection was observed, and the process parameters of sample no. 3 should be the target to receive further evaluation.

However, this condition greatly depends on different process variables. Common weld defects including sagging, pores, and lack of penetration were presented in the other three samples. In sample no. 1, the imperfection of sagging was discovered. It tends to appear on the condition of overheating which results in so much melting metal that the surface tension could not keep the pool in place. Plenty of research has been conducted with the aid of electromagnetic field to suppress drop-outs experimentally and numerically [17, 18]. Sample no. 2 showed narrow hump on the top and intermittent weld on the bottom while lack of penetration was presented by no. 4. Among them, hump was believed to generate for pressure difference along the length of weld pool which is a function of surface tension and curvature [19]. It was commonly seen when high welding speed and large-enough laser power were

utilized. Intermittent weld and lack of penetration were attributed to heat input induced by a high speed or low power.

3.2 Microstructure

The microstructure of A7N01 hybrid welding joint can be observed through an optical metallographic microscope. Figure 4a shows the fusion transition zone (FZ) with a width of nearly 60 μm. In this zone, part of the base metal experienced some degree of remelting, showing dark coarse overheating structure. On the right side, HAZ presented no visible microstructure change under the optical microscope and retained the as-received fibrous processing marks. On the other side, directional columnar solidification structure was oriented to the center with an upward inclination. A typical image of weld center zone microstructure is given by Fig. 4b, and fine dendritic crystalline microstructure with white α-Al matrix and dark second phases were observed, as well as the black micropores. Combining the observation of cross-section areas, it can be concluded that directional columnar crystals nucleated heterogeneously from the half molten state of the FZ under the effect of thermal flow. This kind of coarse columnar crystals accounted for most part of the WZ, and only a small area in the center was covered by the fine dendritic structure.

Scanning electron microscope (SEM) was used to expose the morphology and distribution of porosities in the welding joints. As showed in Fig. 5a, casting defects were still reserved

Fig. 6 Stomatal three-dimensional distribution model of A7N01 hybrid welding joint
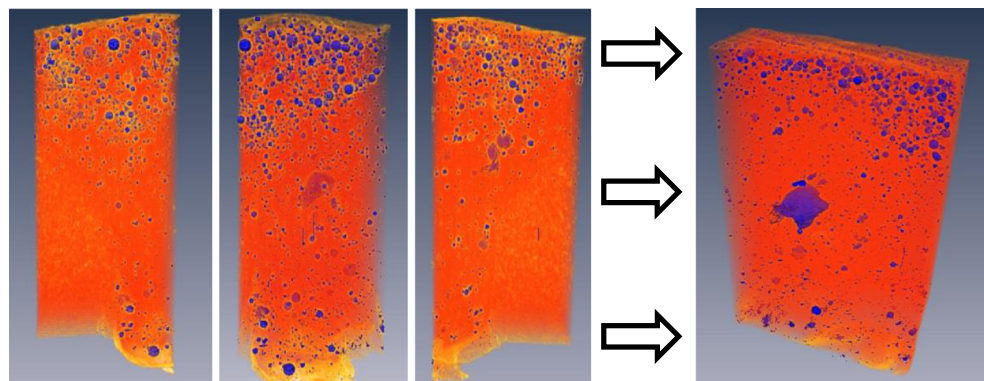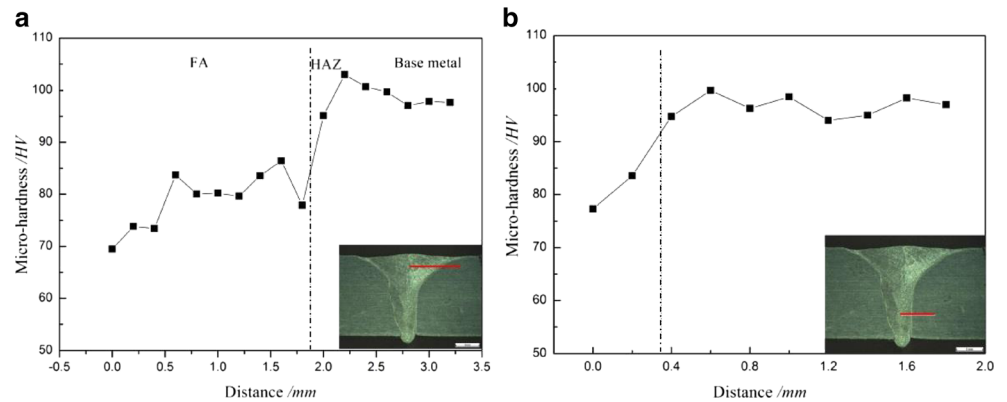
Fig. 7 Microhardness profile of cross section. **a** Laser-arc active region. **b** Laser active region


after heat treatment of T6 and a small amount of pores appeared in BM. Comparatively, Fig. 5c shows that closely packed porosities with diameters of 1–2 μm were found in WZ, which made the weld look like a loose structure. Figure 5b clearly presents this transition near the fusion line, and the sparsity seemed more severe with lots of pores connected in a line. Such porosities should have a great effect on weld performances.

In order to further develop the distribution and morphology of pores, 40 keV synchrotron radiation X-ray microtomography at the 13W1 beamline and station in Shanghai optical source and Amira software were used to build a three-dimensional porosity distribution. The stereogram of the gas porosity inside the weld

joint can be seen in Fig. 6. According to the calculation results, there were altogether 4326 pores in the tested sample, accounting for 0.57 % of the volume fraction and 4.56 % of the cross-sectional area fraction at the most. Nearly spherical pores were dispersed in the whole WZ symmetrically with diameters ranging from 0.1 to 79 μm, among which those larger ones tended to appear near the top and bottom surface. The findings corresponded well with images under microscopes. Plenty of research has been conducted on the porosity formation mechanism and corresponding suppression methods. Pre-welding physical and chemical cleaning, weld preheating and appropriate shielding gas composition are effective ways to restrain this problem to a certain extent. Additionally, there was a huge and angular cavity in the middle of the weld, with

Fig. 8 The element distribution in weld metal. **a** The scanning line. **b** Mg element distribution. **c** Zn element distribution
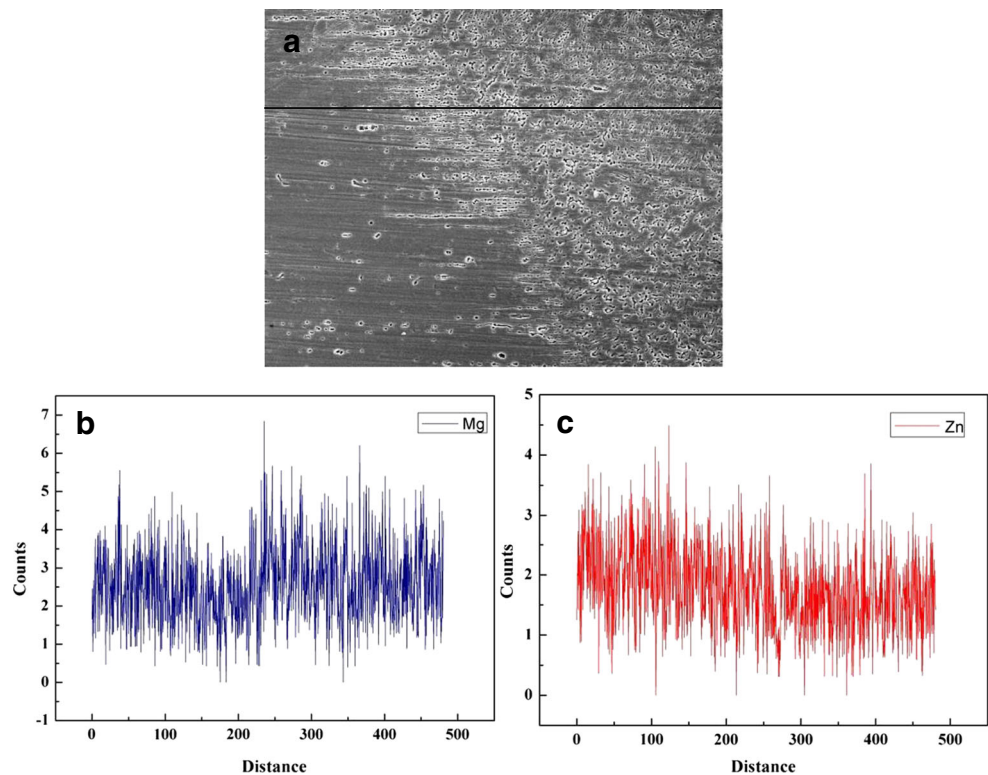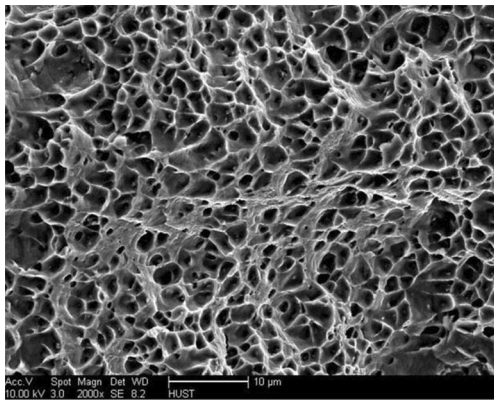
Fig. 9 Fractograph of the BM

apparent incongruity. This defect should not be the hydrogen gas pore and was likely to generate during severe fluctuation of the keyhole.

3.3 Microhardness of welded joints

Figure 7a, b shows the microhardness of the laser-arc and single-laser active region measured along the red line, respectively (the dotted line represented the position of the fusion line). The results suggested that the hardness distribution presented evidently inhomogeneity across the weld. In the laser-arc active region, the mean hardness value of the weld zone was about 76 HV while the average value of 98 HV was found in the base metal. Narrow HAZ (no more than 1 mm in the one-sided width) experienced a drastic change in hardness with a rapid increase up to 104 HV, and then a sharp decrease to the BM level. In the laser active region, the hardness presented a similar increase from FA to BM, but boundaries of HAZ seemed hard to distinguish for its small size, which is common in autogenous laser welding. Apparently, compared with the BM, FA, and HAZ underwent a deep drop in hardness. Moreover, the decrease emerging in the laser-arc active region seemed severer than that in the laser active region.

A7N01-T6 gains its strength by precipitation hardening, which is sensitive to thermal influences [20, 21]. Common strengthening phases consist of η (MgZn$_2$) and T (Al$_2$Mg$_3$Zn$_3$). In general, the higher content and finer

distribution of such phases in the weld, the higher strength, and hardness of the joint. Welding process will also lead to a redistribution of strengthening elements, directly affecting the amount, size, distribution, and morphology of the strengthening phases, and consequently resulting in joint softening. Line scan analysis was performed to investigate the distribution characteristics of main strengthening elements. The measured results conducted in the laser-arc active region are illustrated in Fig. 8. Compared with the BM, content of strengthening element Mg in the WZ had little change, while Zn significantly reduced and could only reach 73 % of the original BM. The former balance was likely due to the effect of supplementary Mg in the filler wire, and the later depletion was believed to generate for evaporation in the heating process considering that the boiling point of Zn approximated 960 °C while the peak temperature of the melt pool surely exceeded this value. Coincidently, hardness value of the weld reached 77.5 % of the BM, which was similar to the decrease percentage of Zn content. It appeared that weld hardness was tightly associated with the distribution of main strengthening elements. Fewer strengthening elements meant fewer strengthening precipitates, leading to weld softening of hybrid welding aluminum alloy. That was to say, dissolution of strengthening precipitates during melting and non-precipitating during quick solidification gave rise to the hardness loss in the WZ. In addition, microporosities formed during solidification in the WZ should also be responsible for the hardness decrease. The HAZ, without suffering from melting and solidification, did not show strengthening element depletion and so many pores as the WZ did. Precipitate coarsening and grain growth, which is the so-called overaging, made HAZ fall somewhere in the middle between the WZ and BM in hardness [22]. And hardness is usually positively associated with tensile strength, which will be discussed in the following.

3.4 Typical tensile fracture

Standard tensile testing of butt welds was performed with the weld bead transversely positioned in the middle of test piece. Welding reinforcement on the weld surface should be eliminated before conducting the test. First, the mechanical

Fig. 10 Mechanism of microvoid accumulation fracture. **a** Micropore nucleation cores. **b** Cores growing up. **c** Microvoid accumulation leading to the connection of dimples
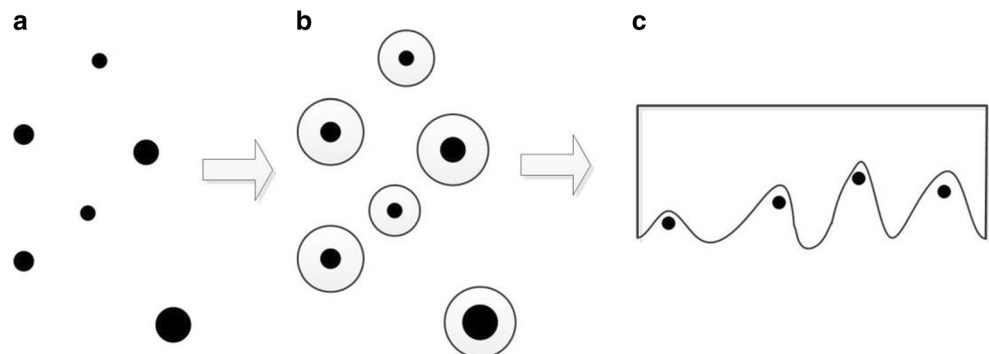
Fig. 11 Tensile specimens welded at the laser power of 3.5 kW, welding speed of 4 m/min, and welding current of 140 A

performance of the BM was tested and the average strength and elongation reached 340 MPa and 11 %, respectively. Typical fractograph is given in Fig. 9. It showed plenty of fine dimples spread uniformly on the fracture surface and presented the features of the so-called equal-axis ductile voids, indicating uniform stress distribution on the fracture. In general, with the increase of the load case, inclusions, precipitations, grain boundaries, and other parts of plastic deformation discontinuity easily become a target area of dislocation accumulation, resulting in local stress concentration and hence micropore nucleation in the area where big local plastic deformation occurs. And further plastic deformation will accelerate these

micropores to grow up and aggregate together until mutual touch and the final rupture [23]. The mechanism of microvoid accumulation fracture (displayed in Fig. 10) and dimple fracture demonstrated that the BM had satisfactory strength and plasticity performances.

Figure 11 shows the results of tensile strength of samples welded under the optimal processing parameters (laser power 3.5 kW, welding speed 4 m/min, and welding current 140 A). A group of three specimens was utilized to avoid accidental error. The average strength of the joints reached 268 MPa, 76.6 % of that of the BM, while elongation came to 6.6 %, 60 % of that of the BM. Among the three typical samples

Fig. 12 Fractograph of welded joints. **a** Overview of tensile fracture surface. **b** Secondary cracks. **c** Step-like small planes. **d** Second-phase particles and pores on the tear edges
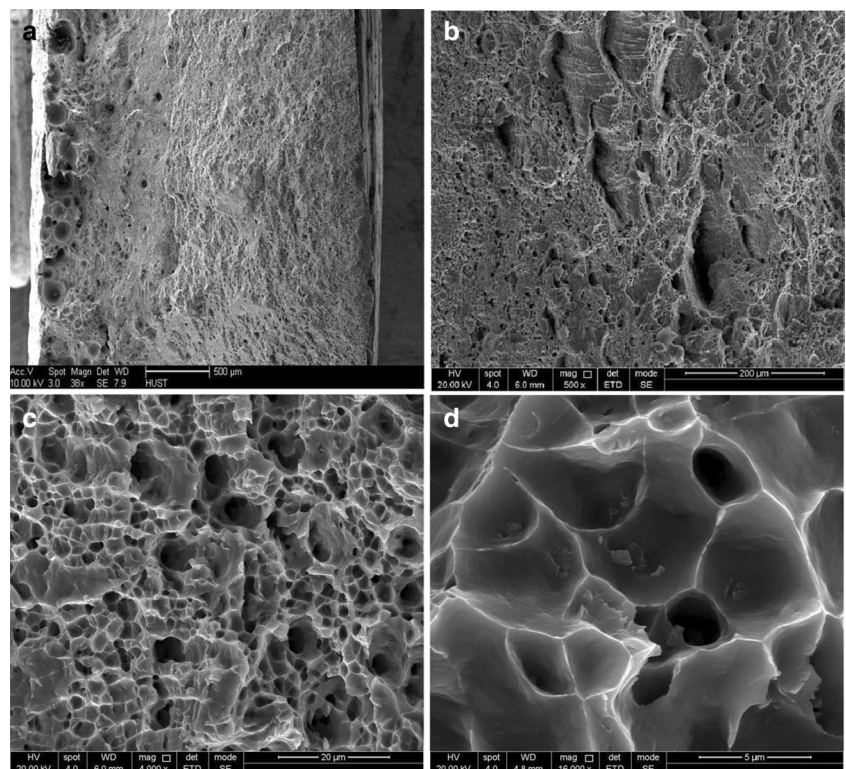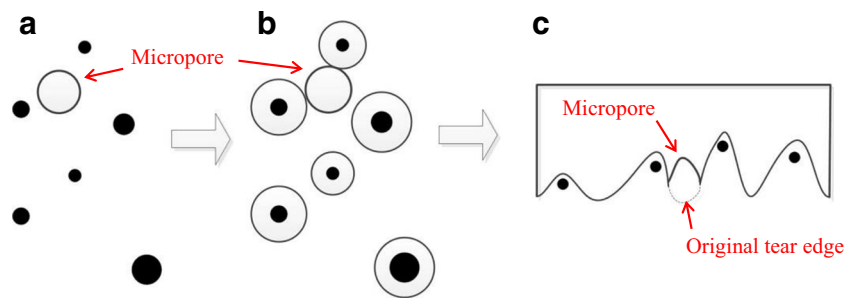
Fig. 13 Effect of micropore on the microvoid accumulation fracture (**a**–**c**)

tested, fracture of welded joints all occurred in the WZ perpendicularly to the axis of tensile, which indicated that the weld seam was the weak point of the joints.

The overview of typical fracture surface of the specimens is shown in Fig. 12a, in which two distinct regions are observed. The left half showed some characteristic features of cleavage and a large number of pores near the surface. Initiation of cracks was also found. Those spherical pores had diameters of no more than 100 μm, which was consistent with the X-ray examination. Dimples were the main morphologies observed in the right half of the joint. Further observation of the right side indicated that there were some secondary cracks shown in Fig. 12b. It is also noteworthy that there were some step-like planes with relative flat surface mixed in the dimples in Fig. 12c, and most of them lay adjacent to pores. In general, secondary cracks and step-like small planes are typical features of quasi-cleavage pattern, in which mode plastic deformation takes place between small planes and small planes are connected with tear ridges. Hence, the right half presented a mixture fracture mode of the quasi-cleavage and ductile.

It can also be observed in Fig. 12d that the second-phase particles with a flaky shape appeared at the bottom of the dimples. In fact, there are always second phases in the multi-element alloys, which can be divided into two categories. One is inclusion, which may disengage from the substrate or split under stress to form microporosity. The other is strengthening phase, such as $MgZn_2$, which always keeps a relatively strong relationship with the substrate. Both of them are likely to be micropore nucleation source. More seriously, some micropores emerged just on the tear ridge between adjacent dimples. Illustrated in Fig. 13, these microdefects generated before tensile experiments are prone to promote premature mutual connection of adjacent dimples. In this condition, dimensions of dimples were decreased, which would have bad effect on the plastic performance of the joints. Therefore, the presence of micropores and second phase particles in the weld seam, on the one hand, would lead to the forming and propagation of cracks for stress concentration and on the other hand, would result in premature contact of dimples, which may be the main reason of facture in advance. Certainly, the absence or weakening of the age-strengthening effect in the FZ and overaging taking place in the HAZ, resulting from the dissolution or

coarsening of fine strengthening precipitates discussed above, should also add to the mismatch of tensile strength. Similarly, this extent of decrease in hardness and strength was also reported in electron beam- or friction stir-welded high-strength aluminum alloys [24, 25].

4 Conclusions

In this paper, laser-metal inert gas (MIG) hybrid welding technique was applied to investigate the weldability of A7N01-T6 aluminum alloy in butt joint configuration. The characteristics of weld morphology, microstructure, element distribution, and their effects on mechanical performances of the joints were analyzed. The main conclusions drawn from this paper are as follows:

1. Welding speed of 4 m/min, laser power of 3.5 kW, and welding current of 140 A are suitable welding parameters for a high-quality A7N01-T6 aluminum alloy laser-MIG welding joint.
2. Fine dendritic crystals in the weld center, columnar dendrites crystals near the fusion line, and as-received fibrous processing marks with no visible microstructure change in HAZ were obtained.
3. Three-dimensional porosity representation by X-ray microtomography indicated that there were altogether 4326 pores with diameters ranging from 0.1 to 79 μm in the tested sample, accounting for 0.57 % of the volume fraction and 4.56 % of the cross-sectional area fraction at the most.
4. The mean hardness of the weld zone was about 76 HV, 77.5 % of that of the BM. The average strength of the joints reached 268 MPa, 76.6 % of that of the BM, while elongation came to 6.6 %, 60 % of that of the BM.
5. The upper half of the joints presented characteristics of brittle fracture, while the bottom half showed a mixture mode of the quasi-cleavage and ductile. Porosities, the dissolution, and coarsening of strengthening precipitates should be responsible for the softening of the joints.

References

1. Dixit M, Mishra R, Sankaran K (2008) Structure-property correlations in Al 7050 and Al 7055 high-strength aluminum alloys. Mater Sci Eng A 478(1):163–172
2. Lakshminarayanan A, Balasubramanian V, Elangovan K (2009) Effect of welding processes on tensile properties of AA6061 aluminium alloy joints. Int J Adv Manuf Technol 40(3):286–296
3. Cam G (2011) Friction stir welded structural materials: beyond Al-alloys. Int Mater Rev 56(1):1–48
4. Malarvizhi S, Raghukandan K, Viswanathan N (2008) Effect of post weld aging treatment on tensile properties of electron beam welded AA2219 aluminum alloy. Int J Adv Manuf Technol 37(3):294–301
5. Cao X, Wanjara P, Huang J, Munro C, Nolting A (2011) Hybrid fiber laser-arc welding of thick section high strength low alloy steel. Mater Des 32(6):3399–3413
6. Möller F, Thomy C (2013) Interaction effects between laser beam and plasma arc in hybrid welding of aluminum. Phys Procedia 41:81–89
7. Enz J, Khomenko V, Riekehr S, Ventzke V, Huber N, Kashaev N (2015) Single-sided laser beam welding of a dissimilar AA2024-AA7050 T-joint. Mater Des 76:110–116
8. Pakdil M, Cam G, Kocak M, Erim S (2011) Microstructural and mechanical characterization of laser beam welded AA6056 Al-alloy. Mater Sci Eng A 528(24):7350–7356
9. Seto N, Katayama S, Matsunawa A (2002) Porosity formation mechanism and reduction method in CO_2 laser welding of stainless steel. Weld Int 16(6):451–460
10. Seto N, Katayama S, Matsunawa A (2000) High-speed simultaneous observation of plasma and keyhole behavior during high power CO2 laser welding: effect of shielding gas on porosity formation. J Laser Appl 12(6):245–250
11. Haboudou A, Peyre P, Vannes A, Peix G (2003) Reduction of porosity content generated during Nd: YAG laser welding of A356 and AA5083 aluminium alloys. Mater Sci Eng A 363(1):40–52
12. Yu YC, Wang CM, Hu XY, Wang J, Yu SF (2010) Porosity in fiber laser formation of 5A06 aluminum alloy. J Mech Sci Technol 24(5):1077–1082
13. Shore R, McCauly R (1970) Effects of porosity on high strength aluminum 7039. Weld J 49(7):311–321
14. Rudy J, Rupert E (1970) Effects of porosity on mechanical properties of aluminum welds. Weld J 49(7):322
15. Gou G, Zhang M, Chen H, Chen J, Li P, Yang YP (2015) Effect of humidity on porosity, microstructure, and fatigue strength of A7N01S-T5 aluminum alloy welded joints in high-speed trains. Mater Des 85:309–317
16. Steen W, Watkins KG, Mazumder J (2010) Laser material processing. Springer-Verlag London, London
17. Li Y, Luo Z, Yan FY, Duan R, Yao Q (2014) Effect of external magnetic field on resistance spot welds of aluminum alloy. Mater Des 56:1025–1033
18. Bachmann M, Avilov V, Gumenyuk A, Rethmeier M (2014) Experimental and numerical investigation of an electromagnetic weld pool support system for high power laser beam welding of austenitic stainless steel. J Mater Process Technol 214(3):578–591
19. Matsunawa A, Ohji T (1982) Role of surface tension in fusion welding (part 1): hydrostatic effect. Trans JWRI 11(2):145–154
20. Balasubramanian V, Ravisankar V, Madhusudhan Reddy G (2008) Effect of pulsed current welding on mechanical properties of high strength aluminum alloy. Int J Adv Manuf Technol 36(3):254–262
21. Katayama S, Ogawa K (2013) Laser weldability and ageing characteristics of welds: laser weldability of commercially available A7N01 alloy (1). Weld Int 27(3):172–183
22. İpekoğlu G, Erim S, Çam G (2014) Effects of temper condition and post weld heat treatment on the microstructure and mechanical properties of friction stir butt-welded AA7075 Al alloy plates. Int J Adv Manuf Technol 70(1):201–213
23. Hull D (1999) Fractography: observing, measuring and interpreting fracture surface topography. Cambridge University Press, Cambridge
24. Kim S, Jeong Y, Park J, Lee Y (2013) Fundamental study on electron beam weld sections and strengths using AA6061-T6 aluminum alloy plate. J Mech Sci Technol 27(10):2935–2940
25. İpekoğlu G, Gören Kıral B, Erim S, Çam G (2012) Investigation of the effect of temper condition on friction stir weldability of AA7075 Al-alloy plates. Mater Technol 46(6):627–632